AIAA SciTech Forum
23-27 January 2023, National Harbor, MD & Online
AIAA SCITECH 2023 Forum

10.2514/6.2023-2385

High-fidelity simulations of plasma-assisted oxidation of hydrocarbon fuels using nanosecond pulsed discharges

Nicholas Deak*, Alfredo Duarte †, Fabrizio Bisetti‡
The University of Texas at Austin, Austin, Texas, 78712

Lucas Esclapez§, Marcus Day ¶
The National Renewable Energy Laboratory, Golden, Colorado, 80401

Next, a robust and efficient framework for simulating NSPD in multiple dimensions is developed. The reactive Navier-Stokes equations are extended to include a drift-diffusion plasma-fluid model with a local field approximation (LFA) in a finite-volume solver, which uses an adaptive mesh refinement (AMR) strategy to address the wide separation of length scales in the problem. A two-way coupling strategy is used whereby the plasma-fluid model and reactive Navier-Stokes equations are integrated simultaneously. The oxidation of ethylene/air mixtures mediated by NSPD is simulated in a pin-to-pin configuration. All phases of the plasma discharge are simulated explicitly (including streamer ignition, propagation, and connection, as well as the subsequent spark phase), along with the evolution of the plasma during the inter-pulse period. Temporally and spatially-resolved results are presented, with an emphasis on the analysis of heating and energy deposition, as well as of the evolution of the concentration of active particles generated during the NSPD and their influence on ignition.

I. Nomenclature

ρ	=	density
$\boldsymbol{u}$	=	bulk gas velocity
p	=	pressure
Π	=	diffusive transport flux for momentum
$\boldsymbol{g}$	=	gravitational acceleration
U	=	Total energy density
$\dot{\omega}_k$	=	production rate of species k
$\boldsymbol{Q}$	=	diffusive transport flux for energy
$\boldsymbol{v}_{\text{eff}}$	=	effective velocity
Y_k	=	mass fraction of species k
$\mathcal{F}_k$	=	diffusive transport flux for species k
z_k	=	charge number of species k
$\boldsymbol{E}$	=	electric field
μ_k	=	mobility of species k
ϕ	=	electric potential
e	=	unit charge
ε_0	=	vacuum permittivity
ρ_c	=	space charge density
S_{ph}	=	photoionization source term
S_{ph}^j	=	photoionization solution component j
p_q	=	quenching pressure

*Graduate Research Assistant, Department of Aerospace Engineering, The University of Texas at Austin.
†Graduate Research Assistant, Department of Aerospace Engineering, The University of Texas at Austin.
‡Professor, Department of Aerospace Engineering, The University of Texas at Austin.
§Researcher, The National Renewable Energy Laboratory.
¶Group Manager III, The National Renewable Energy Laboratory.

S_{ion} = ionization rate
Ψ = photoionization rate function
λ_j = fitting parameter for photoionization solution component j
A_j = fitting parameter for photoionization solution component j
p_{O_2} = partial pressure of oxygen
$\Gamma_{k,x}$ = boundary flux for species k
n_k = number density of species k
γ = secondary electron emission coefficient
$\bar{v}$ = electron thermal velocity
k_B = Boltzmann constant
T_e = electron temperature
m_e = electron mass
E_x = electric field component normal to the boundary
E/N = reduced electric field

II. Introduction

Plasma-assisted ignition (PAI) has emerged in recent years as a promising alternative to traditional ignition [1], relying on the use of low-temperature plasmas (LTP) in place of spark discharges. In particular, nanosecond pulsed discharges (NSPD) have found use in a number of areas due to their ability to enhance ignition and combustion under severe conditions (i.e. ignition of lean and diluted mixtures in internal combustion engines and ultra-lean gas turbines [2–7], supersonic combustion [8, 9]), actuate flow in supersonic environments [10], and promote fuel reforming [11]. The benefits imparted to such systems include thermal heating effects, kinetic enhancements (for instance generation of combustion radicals such as O, H, and OH), and modification of transport properties [12].

NSPD are characterized by an electron temperature that may far exceed the gas temperature $T_e \gg T_g$, along with high applied voltages O(1-100 kV) and reduced electric fields O(100-1000 Td), and short durations O(1-10 ns) [13]. Under such conditions, electrons may attain a mean energy O(1-10 eV), and subsequent collisions with neutral air and hydrocarbon fuel particles may result in the generation of excited species and ions. Of particular importance are the electron collision processes that result in the formation of electronically excited species, which can efficiently generate combustion radicals and promote "fast-heating" [14] of a gas mixture (occurring over tens of nanoseconds), upon relaxation. Also important are electron impact dissociation processes, which directly generate combustion radicals and break down hydrocarbon fuel species, along with electron impact ionization, which is responsible for the creation of additional electrons and ions. The generation of and subsequent relaxation of vibrationally excited species is primarily responsible for "slow-heating" occurring over O(1-10 μs) [15], and may also be of importance when multiple plasma pulses are considered.

Such pulses are often applied between two pin electrodes, resulting in the ignition and subsequent propagation of a plasma streamer, once the applied voltage and resulting electric field are sufficiently strong. Streamer ignition begins near the electrode tips, where the electric field is strongest, forming a cathode-directed positive streamer near the anode, and an anode-directed negative streamer near the cathode. The streamers propagate towards the center of the gap with speeds up of $O(10^5 - 10^7$ m/s) , leaving a near-homogeneous channel of charge-neutral plasma in its wake, with elevated temperature and populations of radicals and excited species. Pulses may be applied until the temperature and radical populations are sufficiently high that an *ignition event* occurs.

Major efforts have been made over to past few decades to better understand and model the broad problem of plasma-assisted combustion. Several experimental studies have focused on developing more accurate kinetics mechanisms describing the interactions of LTP with common hydrocarbon fuels [16–22]. The simulation of streamers in air has also been extensively studied in 2D [23–25], with limited results in 3D as well [26–29]. Numerical studies of PAI in multiple dimensions exist [30, 31], but often rely on simplified kinetics mechanisms and modeling, and use of axisymmetric 2D domains.

This paper seeks to address these limitations by conducting temporally and spatially-resolved axisymmetric simulations of the ignition of application-relevant hydrocarbon/air mixtures via multiple NSPD. First, the ignition and propagation of streamers in air is studied in 3D, using the AMR compressible code PeleC/AMReX. The plasma sheath is characterized, and computational costs are assessed. Finally, the reduced plasma ignition mechanism is used to simulate the ignition of an ethylene/air mixture in 3D.

III. Numerical Model

A. Governing equations

Simulations of the plasma-assisted ignition of ethylene/air mixtures in a pin-to-pin gap are conducted using the reactive Navier-Stokes equations extended to include a drift-diffusion plasma fluid model using two-way coupling, and joule heating effects. The temporal evolution of density, momentum, total energy density, and species mass fractions are modeled as

$$\frac{\partial \rho}{\partial t} = -\nabla \cdot (\rho \boldsymbol{u}) \tag{1}$$

$$\frac{\partial \rho \boldsymbol{u}}{\partial t} = -\nabla \cdot (\rho \boldsymbol{u}\boldsymbol{u} - p\mathcal{I} + \boldsymbol{\Pi}) \tag{2}$$

$$\frac{\partial U}{\partial t} = -\nabla \cdot (\boldsymbol{u}U + p\boldsymbol{u}) + \nabla \cdot \boldsymbol{Q} + en_e\mu_e \boldsymbol{E} \cdot \boldsymbol{E} \tag{3}$$

$$\frac{\partial \rho Y_k}{\partial t} = -\nabla \cdot (\rho(\boldsymbol{u} + z_k\mu_k \boldsymbol{E})Y_k) - \nabla \cdot \boldsymbol{\mathcal{F}}_k + \rho\dot{\omega}_k. \tag{4}$$

Transport equations are modeled for the density ρ, momentum $\rho\boldsymbol{u}$, total energy density ρU, and individual species mass densities ρY_k. Diffusive fluxes for the momentum, energy density, and species mass densities are given as $\boldsymbol{\Pi}$, $\boldsymbol{Q}$, and $\boldsymbol{\mathcal{F}}_k$, while p and $\dot{\omega}_k$ represent pressure and production of species k. Transport coefficients (viscosity, diffusivity, and thermal conductivity) are calculated following Ern and Giovangigli approximations [32]. The velocity of the charged species is calculated as the sum of the bulk velocity $\boldsymbol{u}$, and the drift velocity $z_k\mu_k\boldsymbol{E}$, where z_k and μ_k are the charge number and mobility of species k, and $\boldsymbol{E}$ is the electric field. The electric field is obtained from solving the Poisson problem for the electric potential ϕ

$$\Delta\phi = -\frac{1}{\varepsilon_0}\rho_c, \tag{5}$$

where the charge density $\rho_c = e\sum_k z_k n_k$, and ε_0 is the vacuum permittivity.

Important electron properties, such as the mobility μ_e, diffusivity $\mathcal{D}_e$, temperature T_e, and various rate coefficients are evaluated as functions of the reduced electric field E/N, assuming a local field approximation (LFA) [33]. These quantities have been parameterized as functions of the reduced electric field using data obtained from BOLSIG+ [34]. The BOLSIG+ calculation for electrons in air (modelled as 21% by volume oxygen and balancing nitrogen) was performed using and cross section data from the Morgan database obtained from LXCat [35]. Photoionization effects are modeled using the Zheleznyak approximation [36], and solved using a three-term Helmholtz approximation [37, 38]. It was found in [39] that the presence of hydrocarbons (such as methane) shortens the length of photon propagation, impacting photoionization effects and thus streamer behavior. The impact of such effects on properties such as the streamer ignition time and propagation speed are modest, and are ignored in this work.

The joule heating term is calculated using the unit charge e, the electron number density and mobility n_e and μ_e, and electric field $\boldsymbol{E}$. It is thus assumed that joule heating is primarily driven by the electric field-induced drift of electrons. This is a reasonable assumption, as the transport of ions is slower by several orders of magnitude, due to their much larger size relative to the electron. The diffusion of electrons is also neglected in evaluating the joule heating, as the strong electric fields present during a streamer discharge ensure that drift processes dominate over diffusion. Consistent with the LFA, the electron energy/temperature is a function of the local reduced electric field, and is not modeled separately from the gas energy, as in a local mean energy approximation (LMEA) [40]. It follows that energy gained by the electrons through joule heating effects during the pulse increases the gas energy density instantaneously, which is an approximation. Our previous study [41] conducted using a LMEA demonstrated that for the conditions considered in this paper, pulse energy is first delivered primarily to the electrons. Electrons then transfer energy to the gas through collisions over time scales $O(10\text{ ns})$. As this study is concerned with time scales relevant to ignition and combustion, it is assumed that the error incurred by assuming instantaneous energy deposition is negligible.

A three dimensional domain with electrodes arranged in a pin-to-pin configuration is used for all simulations, conduced using the compressible flow solver PeleC, which uses the adaptive mesh refinement library AMReX [42]. The anode (driven) and cathode (grounded) are located at the top and bottom of the domain, respectively. The pins are modeled as paraboloids, defined by a pin height (fixed at 1.25 mm) and a radius of curvature at the pin tip $r_c = 50\ \mu$m, and a gap length $\ell = 2.5$ mm defined as the distance between the pin tips. Nanosecond pulsed discharges (NSPD) are

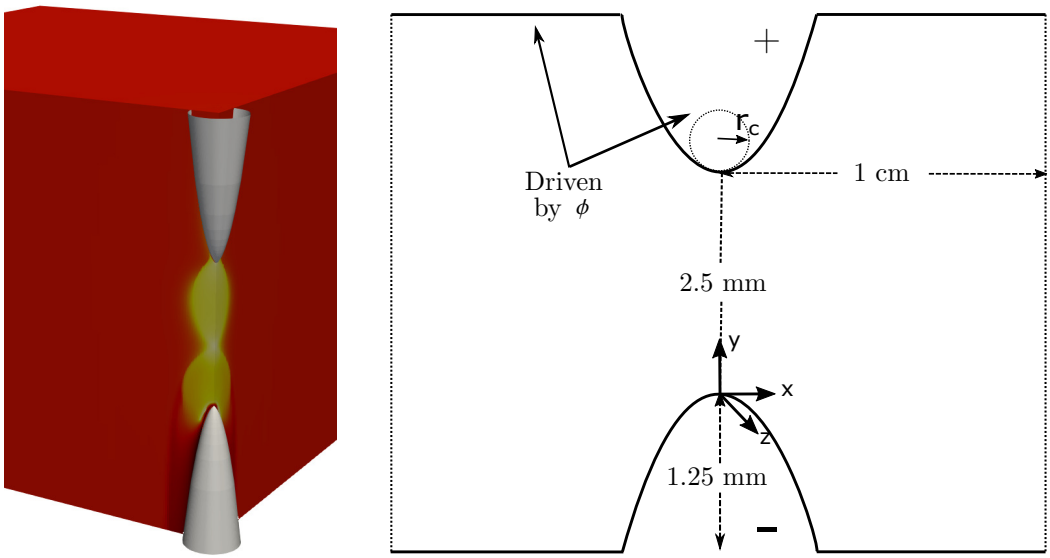

Fig. 1 Electrode configuration; electrode surfaces are represented with solid lines, while far-field boundaries are shown with dotted lines.

applied with a frequency f in order to heat and pressurize the electrode gap region. Each nanosecond discharge is simulated using a time-varying sigmoid voltage signal

$$\phi(t) = \phi_{\max}\left[\sigma(t-\delta,\lambda) + \sigma(t-\delta-T_p-T_r,-\lambda) - 1\right], \tag{6}$$

$$\sigma(t,\lambda) = \frac{1}{1+\mathrm{e}^{-\lambda t}}. \tag{7}$$

Pulse parameters are held constant for all simulations considered, with pulse delay and pulse rise and fall time $\delta = T_r = 2$ ns, pulse plateau time $T_p = 1$ ns, and scaling factor $\lambda = 8/T_r$.

A schematic of the domain is provided in figure 1. In addition to the pins, the top and bottom domain boundaries are treated as electrode surfaces, while the domain boundaries in the span-wise directions are treated as far-field boundaries. Dirichlet conditions are applied for the electric potential at all electrode surfaces, while homogeneous Neumann conditions are applied for charged particles. The pin surfaces are assumed to be adiabatic. Gradients normal to the far-field domain boundaries vanish for all quantities of interest.

B. Electrode surface modeling

Boundary conditions for electrons and ions are taken from [43], marking a modest departure from the conditions typically used in streamer simulations, and are summarized here (assuming, for simplicity, a domain with boundaries oriented in the x direction).

Construction of the boundary conditions follows a "two-stream approximation" [44, 45], which considers both a particle flux directed from the plasma to the wall, and a flux directed from the wall to the plasma. From there, an expression for the electron flux at the electrode boundary ($\Gamma_{e,x}$) is given as

$$\Gamma_{e,x} = \frac{n_e}{2}\bar{v} - 2\gamma\Gamma_{i,x}, \quad \bar{v} = \sqrt{\frac{8k_BT_e}{\pi m_e}}, \tag{8}$$

where $\bar{v}$ is the electron thermal velocity, calculated using the electron temperature and mass (T_e and m_e), along with the Boltzmann constant k_B. Thus, electrons are lost to the electrode boundary through the electron thermal velocity term, and are emitted from the electrode through the secondary electron emission process, dependent on the ion flux to the electrode $\Gamma_{i,x}$, and the secondary electron emission coefficient (SEEC) γ.

Plasma Species	
Vibrational:	N_2(v1), N_2(v2), N_2(v3), N_2(v4), N_2(v5)
Electronic:	$N_2(A^3\Sigma)$, $N_2(B^3\Pi)$, $N_2(C^3\Pi)$, $O_2(a^1\Delta)$, $O_2(b^1\Sigma)$, O(1D)
Charged:	E, N_2^+, O_2^+, O_2^-, O^-

Table 1 Plasma species included in the kinetics mechanism used in this study.

Next, the case of a positive ion is considered, assuming the presence of a strong electric field. Omitting the details, it is shown that the positive ion flux is

$$\Gamma_{i,x} = \begin{cases} n_i V_{d,i}, & \text{if } E_x \geq 0 \\ 0, & \text{otherwise.} \end{cases} \tag{9}$$

An analogous set of conditions can be derived for negative ions, reversing the sign of the electric field. These conditions can be succinctly summarized by noting that if the component of the ion drift velocity normal to the electrode boundary is directed from the plasma to the wall, the ion flux is nonzero and driven by the drift velocity. The ion flux at the electrode surface is zero otherwise. For all charged particles, a zero gradient is assumed at all other domain boundaries.

For the electric potential ϕ, the applied voltage $\phi(t)$ acts as a Dirichlet condition for the driven electrode (in this case the anode), while the grounded electrode (the cathode) uses a zero Dirichlet condition. As before zero gradient conditions are assumed at all other boundaries.

C. Chemical kinetics models

The kinetics mechanism used in [41] and reduced in [46] is used, and describes the plasma-assisted oxidation of ethylene. The original mechanism was comprised of reactions describing plasma processes [19], coupled with the combustion mechanism of [47], and contained 163 species and 1167 reactions, while the reduced mechanism used in this study includes 57 species and 243 reactions. The mechanism includes 5 charged species and 11 excited species (summarized in table 1), and reactions that describe elastic and inelastic collisions between electrons and air/fuel species, resulting in vibrationally and electronically excited air species, dissociation, ionization, and electron-ion recombination. The mechanism from the previous studies has been expanded to include negative ions (O_2^- and O^-), and reactions describing electron attachment and detachment, as well as ion-ion recombination. These reactions are summarized in table 2.

Rxn. No.	Reaction	Fit type	A (cm, s, K, Td)	β	$\delta\varepsilon$ (eV)	Ref.
		Vibrational excitation				
R1	$E + N_2 \rightarrow N_2(v_1) + E$	Janev	4.4×10^{-9}	–	0.29	[19]
R2	$E + N_2 \rightarrow N_2(v_2) + E$	Janev	2.6×10^{-9}	–	0.59	[19]
R3	$E + N_2 \rightarrow N_2(v_3) + E$	Janev	1.8×10^{-9}	–	0.88	[19]
R4	$E + N_2 \rightarrow N_2(v_4) + E$	Janev	1.1×10^{-9}	–	1.17	[19]
R5	$E + N_2 \rightarrow N_2(v_5) + E$	Janev	8.9×10^{-10}	–	1.47	[19]
		Electronic excitation				
R6	$E + N_2 \rightarrow N_2(A^3\Sigma) + E$	Janev	1.8×10^{-10}	–	6.17	[19]
R7	$E + N_2 \rightarrow N_2(B^3\Pi) + E$	Janev	2.1×10^{-9}	–	7.35	[19]
R8	$E + N_2 \rightarrow N_2(C^3\Pi) + E$	Janev	5.5×10^{-9}	–	11.03	[19]
R9	$E + O_2 \rightarrow O_2(a^1\Delta) + E$	Janev	9.6×10^{-10}	–	0.98	[19]
R10	$E + O_2 \rightarrow O_2(b^1\Sigma) + E$	Janev	2.3×10^{-10}	–	1.63	[19]
R11	$E + O \rightarrow O(1\,D) + E$	Janev	3.4×10^{-9}	–	1.97	[19]
		Impact dissociation				
R12	$E + N_2 \rightarrow 2N + E$	Janev	3.4×10^{-8}	–	13.00	[19]
R13	$E + O_2 \rightarrow 2O + E$	Janev	5.9×10^{-10}	–	4.50	[19]
R14	$E + O_2 \rightarrow O + O(1\,D) + E$	Janev	1.8×10^{-9}	–	6.00	[19]
R15	$E + O_2 \rightarrow 2O(1\,D) + E$	Janev	3.1×10^{-8}	–	8.40	[19]
R16	$E + C_2H_4 \rightarrow C_2H_3 + H + E$	Janev	3.7×10^{-9}	–	3.80	[19]
R17	$E + C_2H_2 \rightarrow C_2H + H + E$	Janev	7.6×10^{-9}	–	1.91	[19]
R18	$E + H_2 \rightarrow 2H + E$	Janev	3.9×10^{-9}	–	8.90	[19]
		Ionization				
R19	$E + N_2 \rightarrow N_2^+ + 2E$	$f(E/N)$	3.3×10^{-8}	–	15.60	[48]
R20	$E + O_2 \rightarrow O_2^+ + 2E$	$f(E/N)$	3.9×10^{-8}	–	12.06	[48]
		Electron attachment				
R21	$E + O_2 + M \rightarrow O_2^- + M$	$f(T_e)$	–	–	–	[49]
R22	$E + O_2 \rightarrow O + O^-$	FIT1	8.1×10^{-12}	–	–	[50]
R23	$E + O_2(a^1\Delta) \rightarrow O + O^-$	FIT1	8.7×10^{-11}	–	–	[50]
R24	$E + O_2(b^1\Sigma) \rightarrow O + O^-$	FIT1	2.3×10^{-11}	–	–	[50]
		Charge transfer and electron detachment				
R25	$O^- + O_2 \rightarrow O + O_2^-$	Janev	1.6×10^{-11}	–	–	[51]
R26	$O_2^- + O_2 \rightarrow E + 2O_2$	FIT1	4.2×10^{-10}	–	–	[51]
R27	$O^- + O_2 \rightarrow E + O_2 + O$	FIT1	1.2×10^{-9}	–	–	[51]
R28	$O^- + N_2 \rightarrow E + N_2 + O$	FIT1	2.2×10^{-12}	–	–	[51]
		Electron-ion and ion-ion recombination				
R29	$E + N_2^+ \rightarrow 2N$	Arr.	4.9×10^{-5}	-0.5	–	[19]
R30	$E + O_2^+ \rightarrow 2O$	Arr.	6.0×10^{-4}	-1.0	–	[19]
R31	$O_2^- + O_2^+ + M \rightarrow 2O_2 + M$	Arr.	3.1×10^{-19}	-2.5	–	[49]
R32	$O^- + O_2^+ + M \rightarrow O + O_2 + M$	Arr.	3.1×10^{-19}	-2.5	–	[49]
R33	$O_2^- + N_2^+ + M \rightarrow O_2 + N_2 + M$	Arr.	3.1×10^{-19}	-2.5	–	[49]
R34	$O^- + N_2^+ + M \rightarrow O + N_2 + M$	Arr.	3.1×10^{-19}	-2.5	–	[49]

Table 2 Summary of reactions involving electrons and ions.

The vibrational and electronic excitation, impact dissociation, and ionization forward rate coefficients are functions of the electron temperature T_e, and are fit using the Janev functional form available in CHEMKIN, given as

$$k_f = AT_e^{\beta}\exp\left(\frac{E_i}{T_e}\sum_{j=1}^{9} b_j(\ln T_e)^j\right). \tag{10}$$

The two-body electron attachment and charge transfer and electron detachment functions are also functions of T_e, and

are fit using the FIT1 functional form available in CHEMKIN, given as

$$k_f = AT_e^{\beta} \exp\left(\sum_{j=1}^{4} \frac{b_j}{T_e^j}\right). \tag{11}$$

The electron-ion recombination rate coefficient follows the standard Arrhenius form, and the remaining rate coefficients in table 2 are taken from [49]. The mechanism also describes the quenching of vibrationally and electronically excited species, which are associated with fast [14] and slow [15] heating processes, respectively.

D. Numerical methods

To resolve sharp gradients in the solution (for instance in the streamer head, and near the electrode tips), grid spacing $O(1\ \mu\text{m})$ is required. As these regions are typically limited to a very small percentage of the overall domain, the adaptive mesh refinement (AMR) library AMReX [42] is used to increase the grid resolution in these regions only. A base coarse mesh consisting of cells with a grid spacing $\Delta = 156\ \mu$m in each direction is defined on the entire domain. A hierarchy of successively finer grids are used to resolve steep gradients in the solution, with up to 7 additional levels of refinement (with a refinement factor 2) utilized (resulting in $\Delta_{\text{min}} = 1.25\ \mu$m).

Refinement criteria are defined based on the gradients in the reduced electric field E/N, temperature T, and pressure p. Cells are tagged for refinement at a given level when the absolute value of the finite difference between adjacent cells exceeds a user-specified threshold. For the atmospheric cases discussed in the remainder of this chapter, $\Delta E/N = 50$ Td, $\Delta T = 100$ K, and $\Delta p = 0.05$ atm. These parameters ensure sufficient resolution of the propagating streamer head and resulting plasma channel, as well as the heated and pressured hot spots that form near the electrode tips, and the subsequent shock waves. The pin surfaces are represented using an embedded boundary (EB) approach [52], with a state redistribution scheme [53] used to resolve the small cut cell problem. In order to ensure the EB geometry is resolved adequately, cells that intersect with the surfaces of the electrodes are also tagged for refinement, up to the highest level.

Due to their small mass, time step size constraints are largely driven by the electron dynamics. Specifically, the electron drift Courant-Friedrichs-Lewy (CFL) condition and dielectric relaxation time scale (which is associated with the coupling between changes in the space charge density and electric field) control the stable time step size δt. Following [54], δt is calculated as

$$\delta t = \min(0.3\,\delta t_A, 5.0\,\delta t_E), \tag{12}$$

$$\delta t_A = \min\left(\frac{\Delta}{|\boldsymbol{v}|_{\text{eff},e}}\right), \tag{13}$$

$$\delta t_E = \min\left(\frac{\varepsilon_0}{e\mu_e n_e}\right), \tag{14}$$

where δt_A and δt_E represent the electron drift and dielectric relaxation time scale constraints, and minimization occurs across the entire domain and all AMR levels. The coefficient of 0.3 differs from the original study, driven by requirements of the MOL strategy. The factor of 5.0 is larger by an order of magnitude as well, due to the semi-implicit handling of the Poisson equation[55].

Advection of the conserved variables ($\boldsymbol{U}$) is discretized using a Godunov scheme with characteristic extrapolation to the cell faces, and a Riemann solver. Diffusive sources are discretized using a second-order centered approach, and transport coefficients based on Ern and Giovangigli approximations [32]. Time advancement uses a predictor-corrector approach, whereby the advective and diffusive sources $\boldsymbol{S}_{AD}$ are calculated multiple times in order to construct an approximation to the conserved variable $\boldsymbol{U}^{**}$

$$\boldsymbol{S}_{AD}^{n} = A(\boldsymbol{U}^{n}) + D(\boldsymbol{U}^{n}) \tag{15}$$

$$\boldsymbol{U}^{*} = \boldsymbol{U}^{n} + \Delta t(\boldsymbol{S}_{AD}^{n} + \boldsymbol{\omega}_r) \tag{16}$$

$$\boldsymbol{S}_{AD}^{n+1} = A(\boldsymbol{U}^{*}) + D(\boldsymbol{U}^{*}) \tag{17}$$

$$\boldsymbol{U}^{**} = \frac{1}{2}(\boldsymbol{U}^{n} + \boldsymbol{U}^{*}) + \frac{\Delta t}{2}(\boldsymbol{S}_{AD}^{n+1} + \boldsymbol{\omega}_r), \tag{18}$$

where A and D represent the advective and diffusive operators, while $\boldsymbol{\omega}_r$ is a time-lagged reactive source. From here, an advective/diffusive forcing term is calculated

$$\boldsymbol{F}_{AD} = \frac{1}{\Delta t}(\boldsymbol{U}^{**} - \boldsymbol{u}^{n}) - \boldsymbol{\omega}_r, \tag{19}$$

after which the solution at the next time step is obtained by integrating $\boldsymbol{U}^n$ with $\boldsymbol{F}_{AD}$ and the reactive sources until time $n+1$ using CVODE [56]. The time-lagged reactive source term is then updated for the next time step

$$\boldsymbol{\omega}_r = \frac{\boldsymbol{U}^{n+1} - \boldsymbol{U}^n}{\Delta t} - \boldsymbol{F}_{AD}. \tag{20}$$

The time advancement strategy is summarized in algorithm 1.

Algorithm 1 PeleC advancement framework

procedure ADVANCE($\boldsymbol{U}(\rho, \rho\boldsymbol{u}, U, n_k)$)
  while $t < t_{\text{out}}$ **do**
    $\boldsymbol{E}^{n+1} = -\nabla\phi^{n+1}$ ▷ Applied voltage ϕ_{app} at anode, semi-implicit approx.
    $S_{ph} = S_{ph}(\boldsymbol{U}^n)$ ▷ Calculated using 3-term Helmholtz approx.
    $\boldsymbol{S}^* = AD(\boldsymbol{U}^n, \boldsymbol{E}^{n+1})$ ▷ Advective/diffusive sources and boundary fluxes
      $D_{Y_E} = D(Y_E^n)$ ▷ Implicit evaluation of the Y_E diffusive source
      $S_U^* += S_{jh}(\boldsymbol{U}^n, \boldsymbol{E}^{n+1})$ ▷ Joule heating increases gas energy
    $\boldsymbol{U}^* = \boldsymbol{U}^n + \Delta t(\boldsymbol{S}^* + \boldsymbol{\omega}_r)$
    $\boldsymbol{S}^{n+1} = AD(\boldsymbol{U}^*, \boldsymbol{E}^{n+1})$
      $D_{Y_E} = D(Y_E^*)$
      $S_U^{n+1} += S_{jh}(\boldsymbol{U}^*, \boldsymbol{E}^{n+1})$
    $\boldsymbol{U}^{**} = \frac{1}{2}(\boldsymbol{U}^n + \boldsymbol{U}^*) + \frac{\Delta t}{2}(\boldsymbol{S}^{n+1} + \boldsymbol{\omega}_r)$
    $\boldsymbol{F}_{AD} = \frac{1}{\Delta t}(\boldsymbol{U}^{**} - \boldsymbol{U}^n) - \boldsymbol{\omega}_r$ ▷ Advective/diffusive forcing term
    $\boldsymbol{\omega}_r = \boldsymbol{\omega}_r(\boldsymbol{U}^n, \boldsymbol{F}_{AD}, S_{ph})$ ▷ Integrated using CVODE
    $\boldsymbol{U}^{n+1} = \boldsymbol{U}^n + \Delta t(\boldsymbol{F}_{AD} + \boldsymbol{\omega}_r)$
  end while
end procedure

IV. Results

A. Voltage sensitivity

A zero-dimensional study is performed first to characterize the sensitivity of the solution to the applied voltage. An isochoric and adiabatic reactor with a time-varying applied electric field sigmoid profile in equation 6 is used to ignite the plasma, and the impact on the evolution of plasma properties is examined. A stoichiometric ethylene/air mixture at atmospheric conditions and an initial temperature of 300 K is considered first, and simulations are conducted over an interval of 100 ns. The evolution of the electron number density for various applied electric field strengths is depicted in Fig. 2a, where it is observed that modest changes in the applied electric field strength (~10%) result in important changes in the peak electron number density, which varies by approximately 4 orders of magnitude across cases. This sensitivity extends to the temperature rise ΔT shown in Fig. 2b, which varies from negligible heating for the 70 kV/cm case (not shown) to $O(1000\text{ K})$ for the 80 kV/cm case. The gas heating and electron number densities observed across cases range from values typical of corona discharges to spark discharges.

To understand how this sensitivity changes under conditions that reflect combustion applications, additional cases are run with increasing initial temperature and pressure according to isentropic compression laws

$$\left(\frac{p_1}{p_2}\right) = \left(\frac{T_1}{T_2}\right)^{\frac{\gamma}{\gamma-1}}, \tag{21}$$

with $\gamma = 1.4$. Initial temperatures of $T_0 = 400$, 500, and 600 K are considered. The resulting initial pressures, mass and number densities are provided in table 3. Stronger pulses are required to ignite higher pressure mixtures given the increase in the gas number density. Temporal evolution of the electron number density and gas heating for the 600 K case are provided in Fig. 3. It is again found that small increases in the pulse strength result in substantial changes in the extent of gas heating, with similar sensitivity in the electron number density observed as well.

The sensitivity of the pulse strength on T_0 and p_0 is illustrated in Fig. 4, which shows the change in the gas internal energy density ΔU (at the final time $t = 100$ ns) normalized by the gas number density N, as a function of the reduced

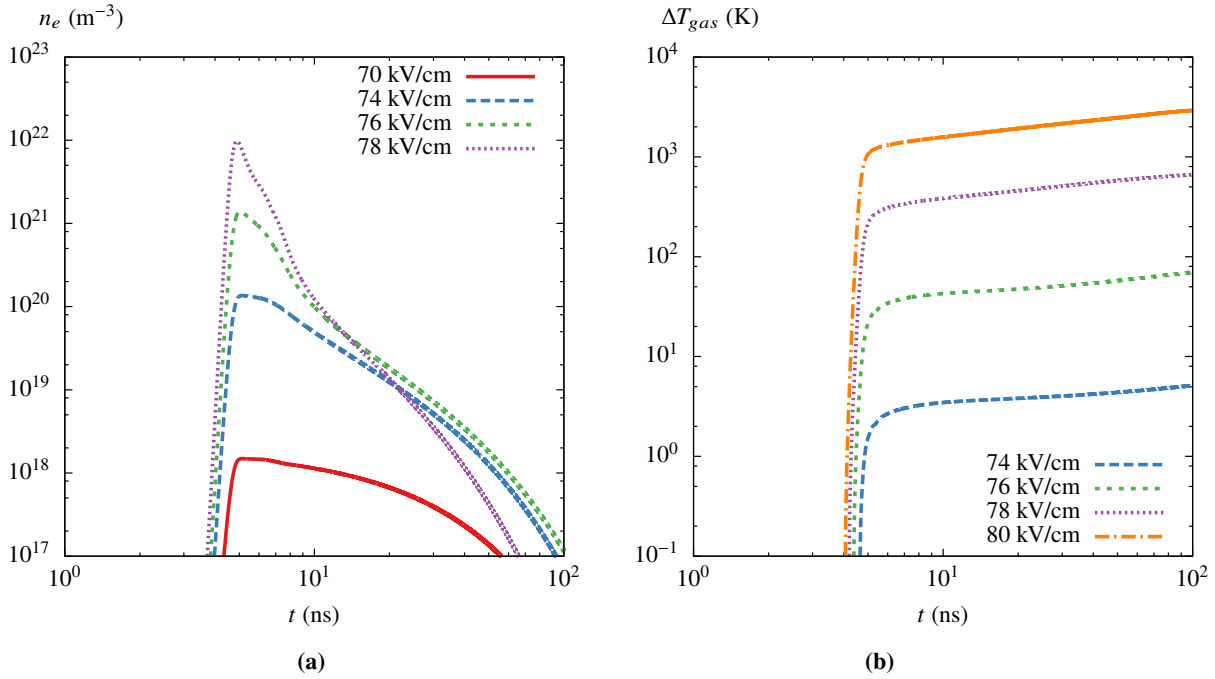

Fig. 2 Temporal evolution of (a) electron number density and (b) gas temperature for various pulse strengths at atmospheric conditions.

T_0 (K)	p_0 (atm)	N (m^{-3})	ρ (kg/m^3)
300	1.0	2.446×10^{25}	1.169
400	2.737	5.022×10^{25}	2.401
500	5.977	8.773×10^{25}	4.194
600	11.314	1.384×10^{26}	6.615

Table 3 Initial conditions used for increasing temperature and pressure PAC streamer cases assuming isentropic compression and stoichiometric ethylene/air.

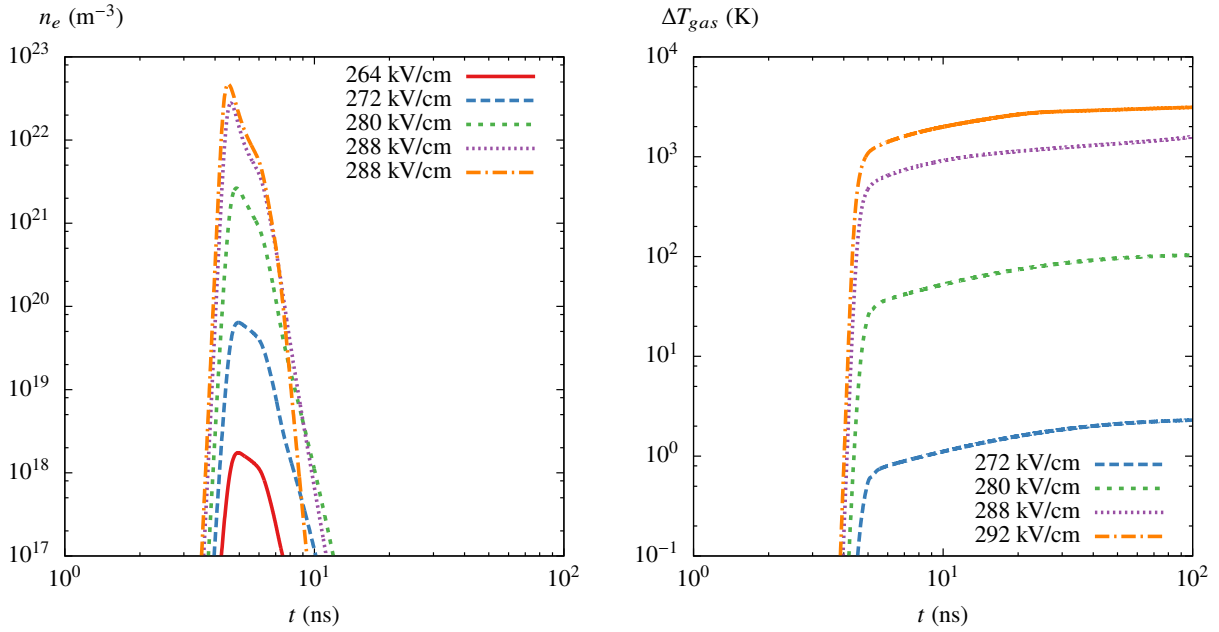

Fig. 3 Temporal evolution of (a) electron number density and (b) gas temperature for various pulse strengths at $T_0 = 600$ K and $p_0 = 11.3$ atm.

electric field. One apparent trend is that as T_0 and p_0 increase, the mixture becomes more sensitive to the pulse strength, as evidenced by the steeper slope for the 11.3 atm case as compared with the atmospheric case. It is also seen that the applied electric field strength corresponding to a given amount of (normalized) deposited energy does not scale linearly with the gas number density, but rather increases at a slower rate. In other words, to obtain the same normalized energy deposition for a case with higher T_0 and p_0, a lower E/N is required, as compared with a lower pressure/temperature case.

While the reactor simulation results cannot be used to directly select parameters for multidimensional discharge simulations, the conclusions drawn suggest that in spatially-resolved simulations of plasma discharges, the discharge regime has a sharp dependence on the pulse strength. The results also provide an indication on how the pulse strength might be adjusted as T_0 and p_0 increase.

B. Single pulse solution

We begin with an overview of the solution during and after a single NSD in section IV.B.1. Next, a detailed analysis of the reactions that contribute most to the production and consumption of combustion radicals is presented in section **??**. Finally, heating and subsequent acoustic expansion in the plasma channel is examined, and ignition theory are used to assess and quantify the conditions necessary for a successful ignition in section **??**.

1. Solution overview

A single pulse is applied to a stoichiometric ethylene/air mixture at atmospheric conditions. The applied voltage was selected to produce a streamer in the glow-to-spark transitional regime, with peak heating of $O(1000$ K). The voltage profile is given as in equation 6, with $\phi_{\max} = 13$ kV. As the applied voltage approaches its peak value, a negative (anode-directed) streamer ignites at the cathode, and a positive (cathode-directed) streamer ignites near the anode at time τ_{ig} (defined as the time at which the peak value of E/N along the axis is observed). The streamers propagate towards the center of the gap and eventually meet at τ_{conn} (defined as the time at which the positive streamer propagates at its peak speed), forming a plasma channel that spans the entire gap. The applied voltage is sustained for a few nanoseconds before dropping during the 2 ns voltage fall phase, which ends by approximately 6 ns.

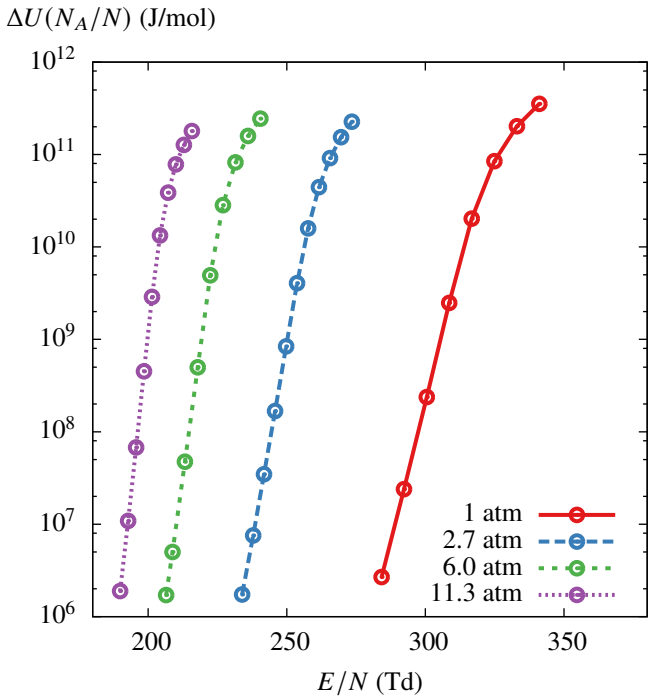

Fig. 4 Deposited energy per particle as a function of the peak reduced electric field strength for the cases outlined in table 3.

As the streamer propagates, strong electric fields in front of the head result in the formation of electrons n_e, cations n_+ (O_2^+ and N_2^+), anions n_- (O_2^-, O^-), vibrationally excited nitrogen $n_{N_2(v)}$ (N_2(v1), N_2(v2), N_2(v3), N_2(v4), N_2(v5)), electronically excited nitrogen $n_{N_2^*}$ ($N_2(A^3\Sigma)$, $N_2(B^3\Pi)$, $N_2(A^3\Sigma)$), metastable oxygen $n_{O_2^*}$ ($O_2(a^1\Delta)$, $O_2(b^1\Sigma)$), combustion radicals n_{rad} (O, OH, and H), and combustion products n_{prod} (CO, CO_2, and H_2O). The solution immediately after the applied voltage is presented in figure 5. The streamer channel is non-uniform radially, with a narrower structure near the anode (top), and a broader more diffuse structure near the cathode (bottom).

As observed in figure 6, the positive and negative streamers propagate with an average speed of approximately 10^6 m/s, in good agreement with values reported in similar studies [24]. Following streamer connection, space charge shielding in the plasma channel results in a nearly uniform electric field across the gap.

It is observed that the most active regions (identified as areas with local maxima in the population of various plasma species) are located near the anode and cathode tips, as well as near the center of the channel (where the positive and negative streamer heads meet and connect to form the plasma channel). The regions near the pin tips are especially active, and undergo rapid heating and pressurization when the applied voltage is sustained after streamer connection. This is driven by local maxima in the reduced electric field strength during the propagation phase, near both the pin tips (due to the pin curvature) as well as in the center of the gap where the streamers.

The increase in temperature near the pin tips is driven by joule heating, as demonstrated in figure 7(a), which shows the temporal evolution of the electron number density and reduced electric field strength at a point near the anode located approximately 1.8 μm from the anode tip axially, and 0.63 μm off the axis of symmetry (referred to as point 1). During the first 2.5 ns of the simulation (prior to streamer ignition), the electric field strength follows the sigmoid profile used to define the applied voltage. Once the positive streamer ignites (at time τ_{ig} = 2.6 ns), the electron number density rapidly increases resulting in space charge shielding and an almost instantaneous reduction in the electric field strength.

There is a transitory phase as the streamers propagate and connect (at time τ_{conn} = 3.7 ns), after which the electron number density further increases by approximately an order of magnitude, eventually reaching a maximum between 4 and 5 ns. It is during this time that a vast majority of the energy is deposited by the pulse, as shown in figure 7(b). The heating of the gas coincides with the energy deposition, and peak temperatures in excess of 2000 K are observed near both the anode and the cathode. The temperature continues to rise even after the energy deposition phase, due primarily to the quenching of electronically nitrogen species, which are responsible for *fast heating* [57].

Detailed insight is provided in figure 8, which shows the streamer solution taken along the axis of symmetry

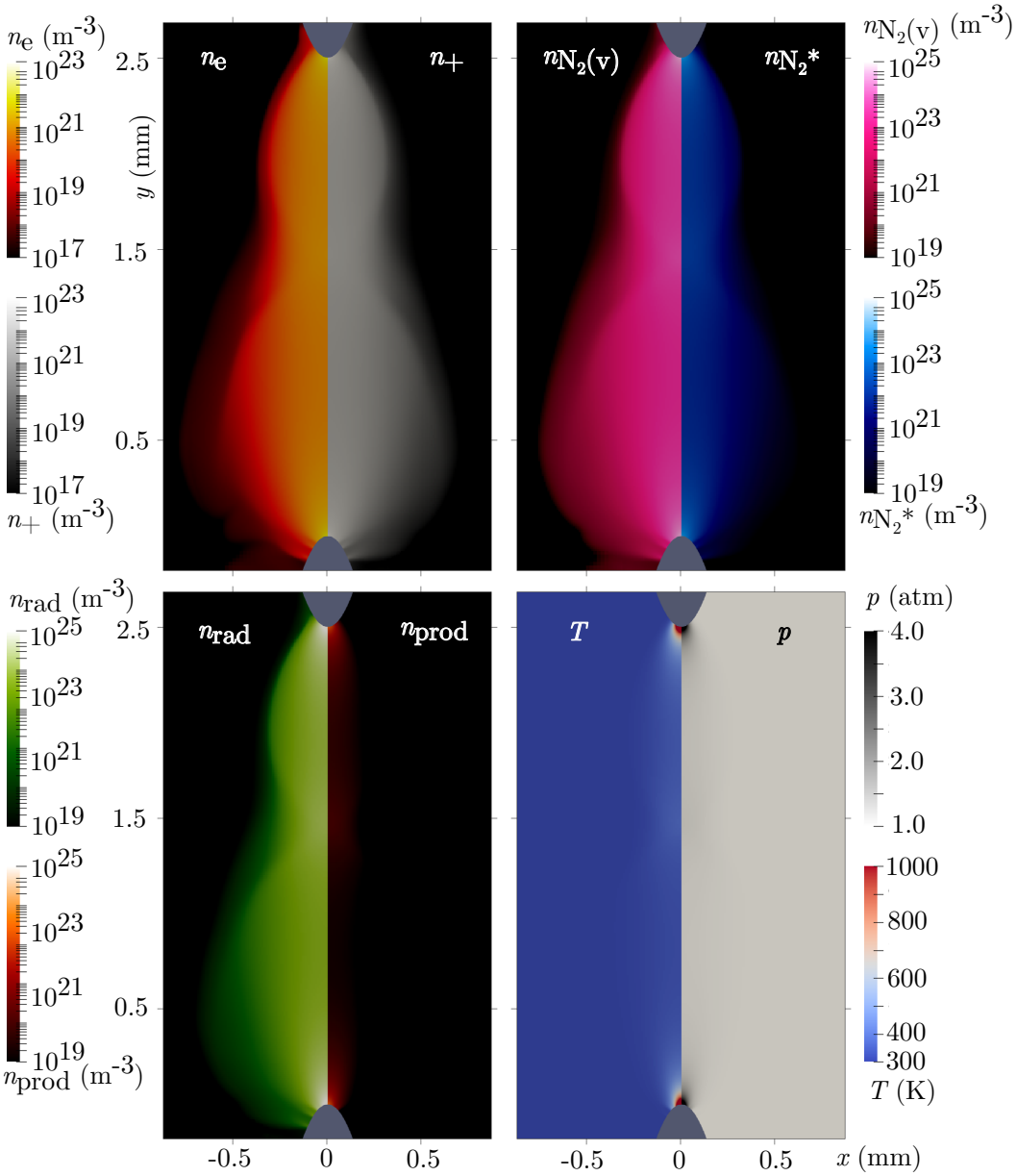

Fig. 5 Streamer solution (n_e, n_+, $n_{N_2(v)}$, $n_{N_2^*}$, n_{rad}, n_{prod}, T, and p) at 6 ns. The plasma channel is comprised of a narrow region formed by the propagation of the positive streamer, and a broader region from by propagation of the negative streamer.

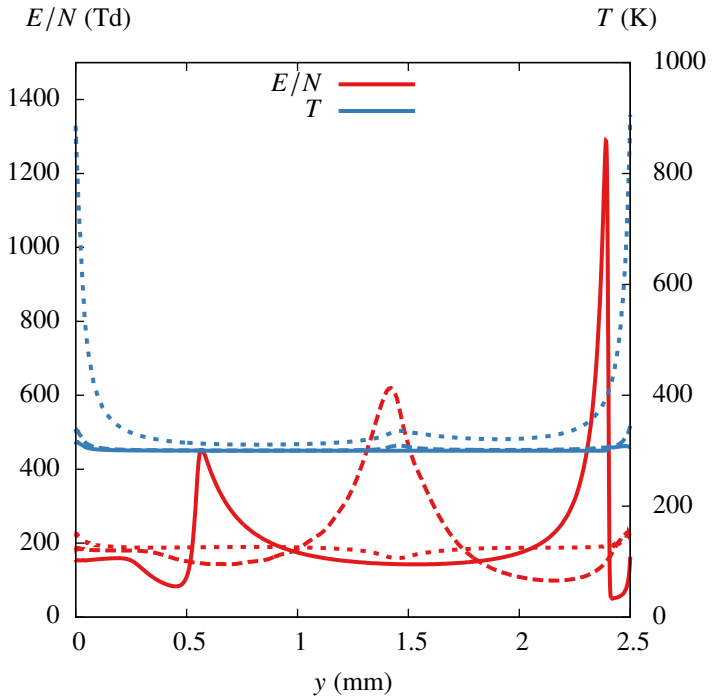

Fig. 6 Reduced electric field and gas temperature along the axis of symmetry at 2.8 ns (solid lines), 3.7 ns (dashed lines), and 4.5 ns (dotted lines). Ignition of the positive streamer occurs at 2.6 ns, while streamer connection occurs at 3.7 ns.

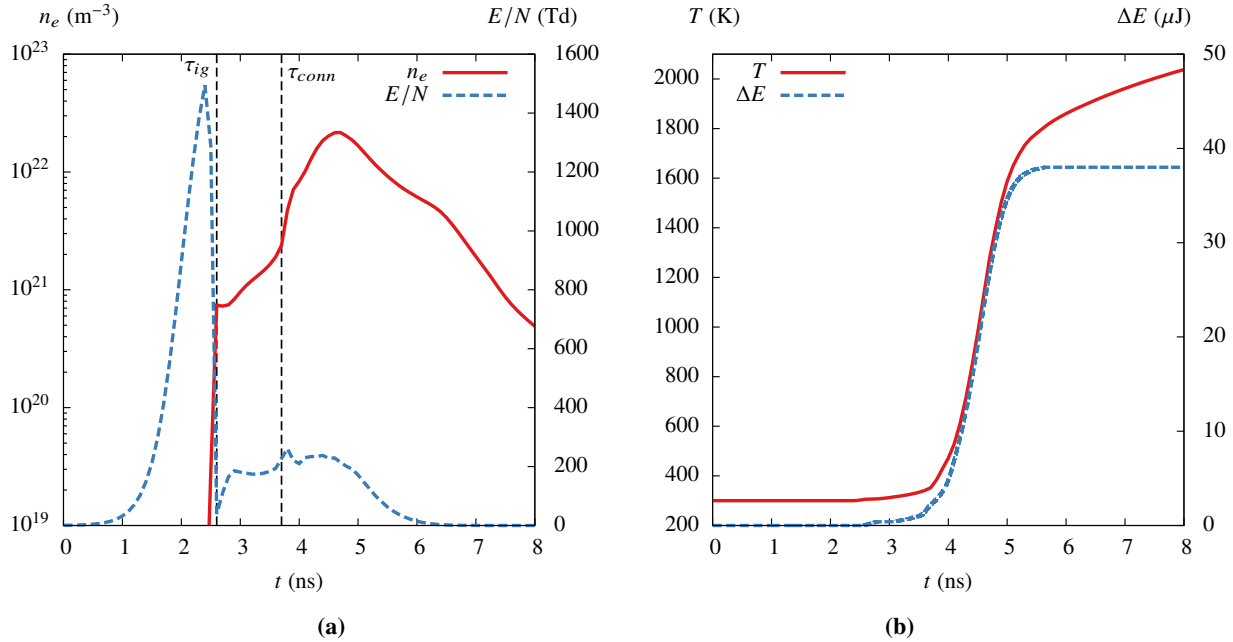

Fig. 7 (a) Temporal evolution of the electron number density and reduced electric field strength at point 1, (b) temporal evolution of the temperature at point 1 and total energy deposited.

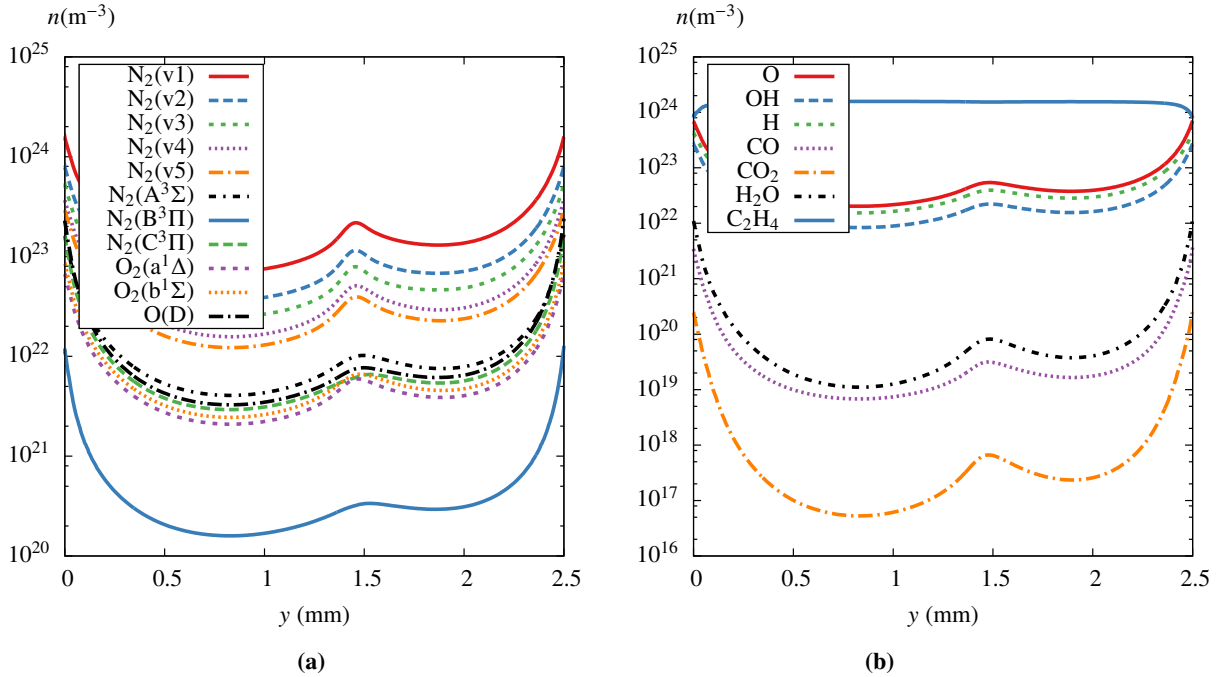

Fig. 8 (a) Number densities of excited state species, (b) number densities of radical and product species along the axis of symmetry at 6 ns.

immediately after the pulse. As noted previously, local maxima are observed near the cathode (y = 0 mm), anode (y = 2.5 mm), and the location where the streamers connect ($y \approx 1.5$ mm). The populations of excited plasma species are provided in figure 8(a). There is a strong correlation between the population of an excited species and its excitation energy $\delta\varepsilon$, whereby species with lower excitation energies are present in greater amount in the plasma channel. This is seen most clearly in the separation between the amount of $n_{N_2(v)}$ (which has excitation energies ranging from 0.29 to 1.47 eV), and the amount of electronically excited species (N_2^*, O_2^*, and O(1D) with excitation energies ranging from 0.98 to 11.03 eV). The population of N_2(v) is one to two orders of magnitude greater than the population of electronically excited species. Likewise, the population of $N_2(v_1)$ (which has the lowest excitation energy) is approximately an order of magnitude higher than the population of $N_2(v_5)$ (which has the highest excitation energy of the vibrationally excited species included in the model).

It is important to distinguish between vibrationally and electronically excited species due to the fact that they play vastly different roles in the context of ignition applications. As previously mentioned, the generation and subsequent quenching of N_2^* is largely responsible for fast heating. This process occurs over O(10 ns), and is responsible for a gas temperature rise of O(10-100 K). As discussed later in section **??**, quenching of N_2^* also plays an important role in combustion radical generation. In contrast, N_2(v) (and long-lived electronically excited species like metastable $O_2(a^1\Delta)$ and $O_2(b^1\Sigma)$) persist for much longer periods of time (≥ 10 μs). The quenching of N_2(v) results in a much slower temperature rise known as *slow heating* [15]. Over shorter periods of time this heating is negligible, and the generation of vibrationally excited species acts as a energy sink, effectively trapping a portion of the pulse energy without any appreciable increase in the gas temperature or generation of combustion radicals.

The population of combustion radicals in the plasma channel is shown in figure 8(b). It is apparent that O is created in the greatest amount, followed by OH and H. This is consistent with previous investigations of LTP chemistry [41], which found that electron impact reactions and electronically excited species quenching primarily results in the formation of O, which in turn promotes the formation of H and OH radicals. Combustion products are also formed immediately following the pulse, albeit in much smaller amounts. The population of CO_2 is lower than the population of CO and H_2O by one to two orders of magnitude. Since conversion of CO to CO_2 is responsible for much of the heat release in conventional hydrocarbon combustion, this indicates that an *ignition event* is not imminent.

The temporal evolution of the solution (anion, cation, N_2(v), N_2^* combustion radical, and combustion product mass densities integrated across the entire domain) over longer periods of time following the pulse is presented in figure 9. The species masses have been normalized using a reference mass $m_{ref} = 2.29619 \times 10^{-6}$ g, which is the mass of the

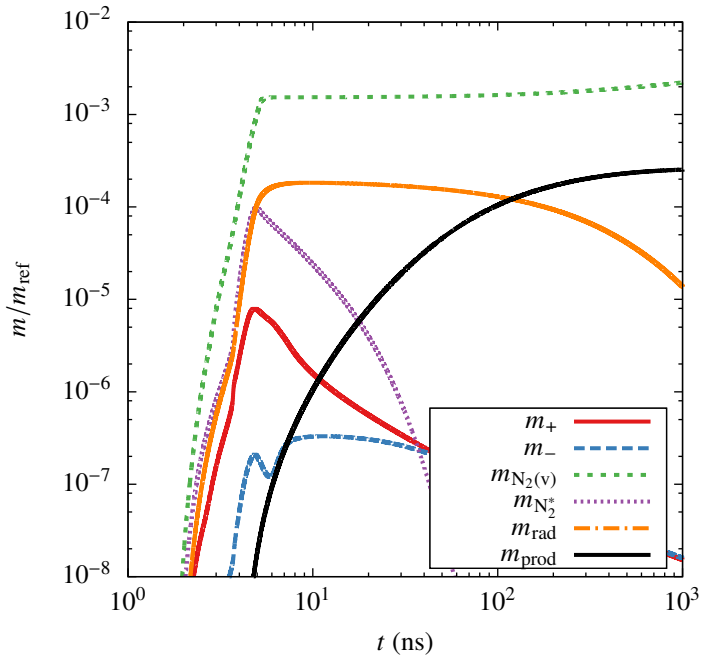

Fig. 9 Temporal evolution of the total amount of cations, anions, vibrationally and electronically excited N_2, radicals, and products integrated across the entire domain, normalized using a reference gas mass $m_{\text{ref}} = 2.29619 \times 10^{-6}$ g.

initial gas mixture in a cylindrical region with a height of 2.5 mm, and a radius of 0.5 mm (approximating the volume occupied by the plasma channel). Following the pulse, there is a transient period during which electrons attach to O_2 and O, after which the concentrations of cations and anions decay primarily due to ion-ion recombination reactions (R31-34). N_2(v) remains present in large amounts long after the pulse, in contrast with N_2^*, which is rapidly quenched after O(10 ns). Combustion radicals are consumed over an interval O(0.1-1 μs). Combustion products (primarily CO and H_2O) are produced both during the pulse and long after, as combustion radicals generated by the discharge are consumed in fuel oxidation reactions.

A more complete picture of the solution is provided by radial profiles at various instances in time and locations across the gap. Two radial profiles are taken across the plane of symmetry: one profile across the top portion of the plasma channel near the anode (y = 0.5 mm from the anode tip), and one across the bottom portion of the channel near the cathode (y = 0.75 mm from the cathode tip). The solutions, provided in figure 10, are taken at three instants in time (t = 10, 100, 1000 ns). Solution profiles taken near the anode are denoted with an "a'' subscript, while solutions near the cathode are denoted with a "c'' subscript.

As apparent in figure 5, the radial extent of the plasma channel near the cathode is greater for all variables of interest. It is also observed that within the portion of the channel formed by the positive streamer (closer to the anode), the population of active species is greater than in the portion formed by the negative streamer (near the cathode). This is due to the fact that the reduced electric field strength in front of the positive streamer is larger than that in front of the negative streamer. This is apparent from the solution at 2.8 ns in figure 6, where the negative and positive streamer heads correspond with the maxima in E/N at $y \approx 0.5$ and $y \approx 2.4$ mm, respectively.

It is especially informative to consider the temporal evolution of these quantities. The population of electrons changes considerably due to electron attachment, decreasing by several orders of magnitude from 10 to 100 ns, and reaching negligible levels by 1 μs. The populations of cations and anions decrease by a few orders of magnitude as well, as ion-ion recombination results in fewer ions over longer periods of time, and transport processes result in a more diffuse structure. Among excited species, significant variation is only observed for N_2^* which decreases considerably from 10 to 100 ns, consistent with the O(10 ns) time scales associated with N_2^* quenching. Given the longer time scales associated with the relaxation of N_2(v) and metastable O_2, almost no variation is observed in the radial profiles for these species.

Combustion radicals are produced during the pulse, after which they are consumed during the inter-pulse period (decreasing in number density by one to two orders of magnitude in the plasma channel), as shown in figure 10(c). Finally, as seen in figure 10(d), the number density of combustion products and gas temperature increase due to fuel oxidation as well as fast and slow heating effects. The increase in the population of combustion products at such low temperatures is possible due to the presence of combustion radicals, which are present largely due to electron impact reactions, and N_2^* quenching. This highlights one of the primary benefits of using LTP in the ignition process. Combustion radicals are not present in such large amounts at low temperatures during traditional thermal ignition. Instead, conventional ignition requires that the gas temperature increase until chain branching leads to the production of combustion radicals, and fuel oxidation.

V. Conclusions

A robust and efficient reactive Navier-Stokes solver was extended to include a plasma-fluid model, while a local field approximation was used to parameterize electron transport coefficients and rate coefficients for electron reactions as functions of the reduced electric field. A two-way coupling strategy was used to ensure that plasma and reactive transport processes interacted with each other throughout the discharge and inter-pulse period. An AMR strategy was used to ensure that large gradients in the reduced electric field strength, pressure, and temperature (which correspond with important physical structures in the discharge solution) were resolved while maintaining a manageable problem size. A skeletal ethylene/air mechanism capable of describing both plasma and combustion kinetics was incorporated into the solver.

First, a sensitivity analysis was performed to assess the impact of voltage strength on the temporal evolution of the solution. A zero-dimensional isochoric and adiabatic reactor was used to simulate plasma discharges via a time-varying electric field strength with a sigmoid profile, and a range of peak voltages. Several simulations at atmospheric conditions were conducted, and it was observed that modest changes in the peak voltage ($\sim 10\%$) produced enormous changes in the discharge characteristics, which ranged from having negligible heating and energy deposition (characteristic of corona discharges), to having significant heating $O(1000\ \mathrm{K})$ and energy deposition (characteristic of spark discharges). The degree of sensitivity to voltage strength was also found to increase at elevated temperatures and pressures.

Next, axisymmetric pin-to-pin plasma discharges in stoichiometric ethylene/air mixtures were simulated through the entire evolution of the streamer (including streamer ignition, propagation, and connection phases, as well as the subsequent spark phase) and through the inter-pulse phase. A single-pulse simulation at atmospheric conditions was conducted using a voltage pulse with a peak of $\phi_{\max} = 13$ kV, which was sufficient to induce a temperature rise of approximately 2000 K near the electrode tips during the spark phase. The solution was then examined through the first 2 μs of the simulation. The composition of the plasma channel was discussed in detail and it was shown that following the pulse, vibrationally excited N_2 dominated the population of excited state species, while the production of O dominated radical production. A peak temperature rise of approximately 2000 K near the pin tips, and a total energy deposition of 38 μJ were observed for the single-pulse case.

Acknowledgments

This research was supported by DOE contract DE-EE0008874, along with computation resources provided by the Texas Advanced Computing Center and National Renewable Energy Laboratory.

References

[1] Ju, Y., and Sun, W., "Plasma assisted combustion: Dynamics and chemistry," *Prog. Energy Combust. Sci.*, Vol. 48, 2015, pp. 21–83.

[2] Serbin, S., Mostipanenko, A., Matveev, I., and Topina, A., "Improvement of the gas turbine plasma assisted combustor characteristics," *49th AIAA aerospace sciences meeting including the new horizons forum and aerospace exposition*, 2011, p. 61.

[3] Santner, J., Dryer, F. L., and Ju, Y., "The effects of water dilution on hydrogen, syngas, and ethylene flames at elevated pressure," *Proceedings of the Combustion Institute*, Vol. 34, No. 1, 2013, pp. 719–726.

[4] Moeck, J., Lacoste, D., Laux, C., and Paschereit, C., "Control of combustion dynamics in a swirl-stabilized combustor with nanosecond repetitively pulsed discharges," *51st AIAA Aerospace Sciences Meeting including the New Horizons Forum and Aerospace Exposition*, 2013, p. 565.

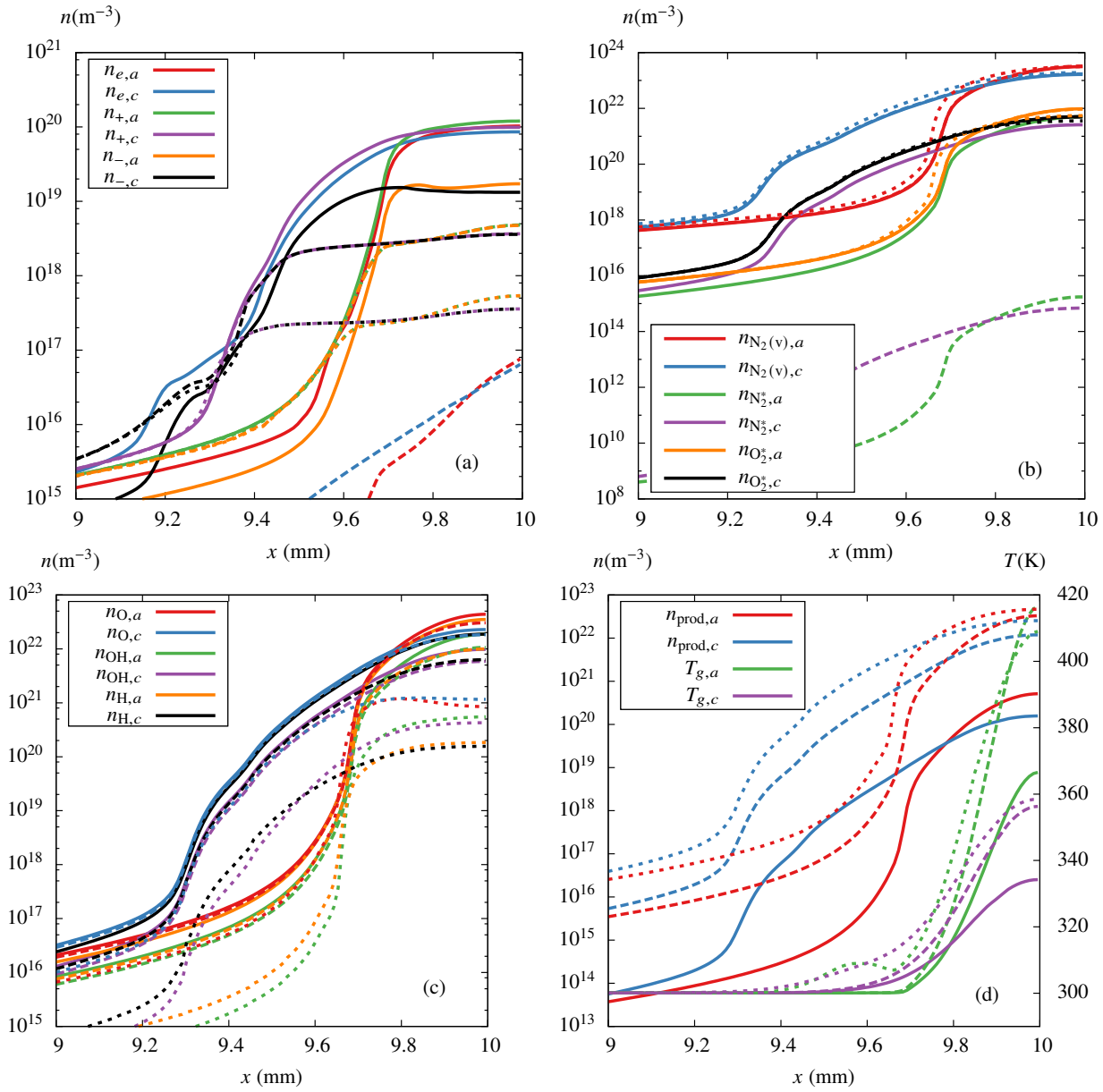

Fig. 10 Radial profiles of the (a) charged particle number density, (b)excited species number density, (c) combustion radical number density, and (d) product number density and gas temperature, taken across the upper and lower portions of the plasma channel at 10 ns (solid), 100 ns (dashed), and 1 μs (dotted).

[5] Sevik, J., Wallner, T., Pamminger, M., Scarcelli, R., Singleton, D., and Sanders, J., "Extending lean and exhaust gas recirculation-dilute operating limits of a modern gasoline direct-injection engine using a low-energy transient plasma ignition system," *J. Eng. Gas Turbine Power*, Vol. 138, No. 11, 2016.

[6] Shiraishi, T., Urushihara, T., and Gundersen, M., "A trial of ignition innovation of gasoline engine by nanosecond pulsed low temperature plasma ignition," *J. Phys. D: Appl. Phys.*, Vol. 42, No. 13, 2009, p. 135208.

[7] Khacef, A., Cormier, J. M., and Pouvesle, J. M., "NOx remediation in oxygen-rich exhaust gas using atmospheric pressure non-thermal plasma generated by a pulsed nanosecond dielectric barrier discharge," *J. Phys. D: Appl. Phys.*, Vol. 35, No. 13, 2002, p. 1491.

[8] Leonov, S. B., and Yarantsev, D. A., "Plasma-induced ignition and plasma-assisted combustion in high-speed flow," *Plasma Sources Sci. Technol.*, Vol. 16, No. 1, 2006, p. 132.

[9] Lefkowitz, J. K., and Ombrello, T., "Reduction of flame development time in nanosecond pulsed high frequency discharge ignition of flowing mixtures," *Combust. Flame*, Vol. 193, 2018, pp. 471–480.

[10] Starikovskii, A. Y., Nikipelov, A., Nudnova, M., and Roupassov, D., "SDBD plasma actuator with nanosecond pulse-periodic discharge," *Plasma Sources Sci. Technol.*, Vol. 18, No. 3, 2009, p. 034015.

[11] Kim, W., Mungal, M. G., and Cappelli, M. A., "The role of in situ reforming in plasma enhanced ultra lean premixed methane/air flames," *Combust. Flame*, Vol. 157, No. 2, 2010, pp. 374–383.

[12] Ju, Y., Lefkowitz, J. K., Reuter, C. B., Won, S. H., Yang, X., Yang, S., Sun, W., Jiang, Z., and Chen, Q., "Plasma assisted low temperature combustion," *Plasma Chem. Plasma Process.*, Vol. 36, No. 1, 2016, pp. 85–105.

[13] Starikovskaia, S. M., "Plasma assisted ignition and combustion," *J. Phys. D: Appl. Phys.*, Vol. 39, No. 16, 2006, p. R265.

[14] Popov, N., "Fast gas heating in a nitrogen–oxygen discharge plasma: I. Kinetic mechanism," *J. Phys. D: Appl. Phys.*, Vol. 44, No. 28, 2011, p. 285201.

[15] Lanier, S., Shkurenkov, I., Adamovich, I. V., and Lempert, W. R., "Two-stage energy thermalization mechanism in nanosecond pulse discharges in air and hydrogen–air mixtures," *Plasma Sources Science and Technology*, Vol. 24, No. 2, 2015, p. 025005.

[16] Togai, K., Tsolas, N., and Yetter, R. A., "Kinetic modeling and sensitivity analysis of plasma-assisted oxidation in a H2/O2/Ar mixture," *Combust. Flame*, Vol. 164, 2016, pp. 239–249.

[17] Winters, C., Eckert, Z., Yin, Z., Frederickson, K., and Adamovich, I., "Measurements and kinetic modeling of atomic species in fuel-oxidizer mixtures excited by a repetitive nanosecond pulse discharge," *J. Phys. D: Appl. Phys.*, Vol. 51, No. 1, 2017, p. 015202.

[18] Winters, C., Hung, Y.-C., Jans, E., Eckert, Z., Frederickson, K., Adamovich, I. V., and Popov, N., "OH radical kinetics in hydrogen-air mixtures at the conditions of strong vibrational nonequilibrium," *J. Phys. D: Appl. Phys.*, Vol. 50, No. 50, 2017, p. 505203.

[19] Eckert, Z. S., "Energy Transfer in Non-Equilibrium Reacting Gas Flows: Applications in Plasma Assisted Combustion and Chemical Gas Lasers," Ph.D. thesis, The Ohio State University, 2018.

[20] Yang, S., Gao, X., Yang, V., Sun, W., Nagaraja, S., Lefkowitz, J. K., and Ju, Y., "Nanosecond pulsed plasma activated C2H4/O2/Ar mixtures in a flow reactor," *J. Propul. Power*, 2016, pp. 1240–1252.

[21] Lefkowitz, J. K., Guo, P., Rousso, A., and Ju, Y., "Species and temperature measurements of methane oxidation in a nanosecond repetitively pulsed discharge," Vol. 373, No. 2048, 2015, p. 20140333.

[22] Rousso, A., Mao, X., Chen, Q., and Ju, Y., "Kinetic studies and mechanism development of plasma assisted pentane combustion," *Proc. Combust. Inst.*, Vol. 37, No. 4, 2019, pp. 5595–5603.

[23] Pancheshnyi, S., and Starikovskii, A. Y., "Two-dimensional numerical modelling of the cathode-directed streamer development in a long gap at high voltage," *J. Phys. D: Appl. Phys.*, Vol. 36, No. 21, 2003, p. 2683.

[24] Tholin, F., and Bourdon, A., "Influence of temperature on the glow regime of a discharge in air at atmospheric pressure between two point electrodes," *J. Phys. D: Appl. Phys.*, Vol. 44, No. 38, 2011, p. 385203.

[25] Zakari, M., Caquineau, H., Hotmar, P., and Ségur, P., "An axisymmetric unstructured finite volume method applied to the numerical modeling of an atmospheric pressure gas discharge," *J. Comput. Phys.*, Vol. 281, 2015, pp. 473–492.

[26] Marskar, R., "An adaptive Cartesian embedded boundary approach for fluid simulations of two-and three-dimensional low temperature plasma filaments in complex geometries," *J. Comput. Phys.*, Vol. 388, 2019, pp. 624–654.

[27] Marskar, R., "3D fluid modeling of positive streamer discharges in air with stochastic photoionization," *Plasma Sources Sci. Technol.*, Vol. 29, No. 5, 2020, p. 055007.

[28] Plewa, J., Eichwald, O., Ducasse, O., Dessante, P., Jacobs, C., Renon, N., and Yousfi, M., "3D streamers simulation in a pin to plane configuration using massively parallel computing," *J. Phys. D: Appl. Phys.*, Vol. 51, No. 9, 2018, p. 095206.

[29] Teunissen, J., and Ebert, U., "Simulating streamer discharges in 3D with the parallel adaptive Afivo framework," *J. Phys. D: Appl. Phys.*, Vol. 50, No. 47, 2017, p. 474001.

[30] Kobayashi, S., Bonaventura, Z., Tholin, F., Popov, N. A., and Bourdon, A., "Study of nanosecond discharges in H2–air mixtures at atmospheric pressure for plasma assisted combustion applications," *Plasma Sources Sci. Technol.*, Vol. 26, No. 7, 2017, p. 075004.

[31] Sharma, A., Subramaniam, V., Solmaz, E., and Raja, L. L., "Fully coupled modeling of nanosecond pulsed plasma assisted combustion ignition," *J. Phys. D: Appl. Phys.*, Vol. 52, No. 9, 2018, p. 095204.

[32] Ern, A., and Giovangigli, V., *Multicomponent transport algorithms*, Vol. 24, Springer Science & Business Media, 1994.

[33] Ward, A., "Calculations of cathode-fall characteristics," *J. Appl. Phys.*, Vol. 33, No. 9, 1962, pp. 2789–2794.

[34] Hagelaar, G., and Pitchford, L., "Solving the Boltzmann equation to obtain electron transport coefficients and rate coefficients for fluid models," *Plasma Sources Sci. Technol.*, Vol. 14, No. 4, 2005, p. 722.

[35] Pancheshnyi, S., Biagi, S., Bordage, M., Hagelaar, G., Morgan, W., Phelps, A., and Pitchford, L., "The LXCat project: Electron scattering cross sections and swarm parameters for low temperature plasma modeling," *Chem. Phys.*, Vol. 398, 2012, pp. 148–153.

[36] Zhelezniak, M., Mnatsakanian, A. K., and Sizykh, S. V., "Photoionization of nitrogen and oxygen mixtures by radiation from a gas discharge," *High Temp.*, Vol. 20, No. 3, 1982, pp. 357–362.

[37] Luque, A., Ebert, U., Montijn, C., and Hundsdorfer, W., "Photoionization in negative streamers: Fast computations and two propagation modes," *Appl. Phys.*, Vol. 90, No. 8, 2007, p. 081501.

[38] Bourdon, A., Pasko, V., Liu, N., Célestin, S., Ségur, P., and Marode, E., "Efficient models for photoionization produced by non-thermal gas discharges in air based on radiative transfer and the Helmholtz equations," *Plasma Sources Sci. Technol.*, Vol. 16, No. 3, 2007, p. 656.

[39] Naidis, G., "Modelling of transient plasma discharges in atmospheric-pressure methane–air mixtures," *J. Phys. D: Appl. Phys.*, Vol. 40, No. 15, 2007, p. 4525.

[40] Park, S.-K., and Economou, D. J., "Analysis of low pressure rf glow discharges using a continuum model," *J. Appl. Phys.*, Vol. 68, No. 8, 1990, pp. 3904–3915.

[41] Deak, N., Bellemans, A., and Bisetti, F., "Plasma-assisted ignition of methane/air and ethylene/air mixtures: Efficiency at low and high pressures," *Proceedings of the Combustion Institute*, Vol. 38, No. 4, 2021, pp. 6551–6558.

[42] Sitaraman, H., Yellapantula, S., de Frahan, M. T. H., Perry, B., Rood, J., Grout, R., and Day, M., "Adaptive mesh based combustion simulations of direct fuel injection effects in a supersonic cavity flame-holder," *Combust. Flame*, Vol. 232, 2021, p. 111531.

[43] Gorin, V., Kudryavtsev, A., Yao, J., Yuan, C., and Zhou, Z., "Boundary conditions for drift-diffusion equations in gas-discharge plasmas," *Phys. Plasmas*, Vol. 27, No. 1, 2020, p. 013505.

[44] Phelps, A., "The diffusion of charged particles in collisional plasmas: free and ambipolar diffusion at low and moderate pressures," *J. Res. Natl. Inst.*, Vol. 95, No. 4, 1990, p. 407.

[45] Chantry, P., Phelps, A., and Schulz, G., "Theory of electron collision experiments at intermediate and high gas densities," *Phys. Rev.*, Vol. 152, No. 1, 1966, p. 81.

[46] Bellemans, A., Kincaid, N., Deak, N., Pepiot, P., and Bisetti, F., "P-DRGEP: a novel methodology for the reduction of kinetics mechanisms for plasma-assisted combustion applications," *Proceedings of the Combustion Institute*, Vol. 38, No. 4, 2021, pp. 6631–6639.

[47] Konnov, A. A., "Implementation of the NCN pathway of prompt-NO formation in the detailed reaction mechanism," *Combust. Flame*, Vol. 156, No. 11, 2009, pp. 2093–2105.

[48] Lowke, J. J., and Morrow, R., "Theoretical analysis of removal of oxides of sulphur and nitrogen in pulsed operation of electrostatic precipitators," *IEEE Trans. Plasma Sci.*, Vol. 23, No. 4, 1995, pp. 661–671.

[49] Kossyi, I., Kostinsky, A. Y., Matveyev, A., and Silakov, V., "Kinetic scheme of the non-equilibrium discharge in nitrogen-oxygen mixtures," *Plasma Sources Sci. Technol.*, Vol. 1, No. 3, 1992, p. 207.

[50] Ionin, A., Kochetov, I., Napartovich, A., and Yuryshev, N., "Physics and engineering of singlet delta oxygen production in low-temperature plasma," *J. Phys. D: Appl. Phys.*, Vol. 40, No. 2, 2007, p. R25.

[51] Ponomarev, A., and Aleksandrov, N., "Monte Carlo simulation of negative ion kinetics in air plasmas in a time-varying electric field," *J. Phys. D: Appl. Phys.*, Vol. 53, No. 5, 2019, p. 055203.

[52] Johansen, H., and Colella, P., "A Cartesian grid embedded boundary method for Poisson's equation on irregular domains," *J. Comput. Phys.*, Vol. 147, No. 1, 1998, pp. 60–85.

[53] Berger, M., and Giuliani, A., "A state redistribution algorithm for finite volume schemes on cut cell meshes," *J. Comput. Phys.*, Vol. 428, 2021, p. 109820.

[54] Vitello, P., Penetrante, B., and Bardsley, J., "Simulation of negative-streamer dynamics in nitrogen," *Phys. Rev. E*, Vol. 49, No. 6, 1994, p. 5574.

[55] Ventzek, P. L., Sommerer, T. J., Hoekstra, R. J., and Kushner, M. J., "Two-dimensional hybrid model of inductively coupled plasma sources for etching," *Appl. Phys.*, Vol. 63, No. 5, 1993, pp. 605–607.

[56] Hindmarsh, A. C., Brown, P. N., Grant, K. E., Lee, S. L., Serban, R., Shumaker, D. E., and Woodward, C. S., "SUNDIALS: Suite of nonlinear and differential/algebraic equation solvers," *ACM Trans. Math. Software*, Vol. 31, No. 3, 2005, pp. 363–396.

[57] Shkurenkov, I., and Adamovich, I. V., "Energy balance in nanosecond pulse discharges in nitrogen and air," *Plasma Sources Sci. Technol.*, Vol. 25, No. 1, 2016, p. 015021.